

# Machine Learning Approach to Detect Arc Faults Based on Regular Coupling Features

Run Jiang, Guanghai Bao, Qiteng Hong and Campbell D. Booth

**Abstract**—During AC series arc faults (SAFs), arcing current features can change significantly or vanish rapidly under different load-combination modes and fault inception points. The phenomena make it very challenging for feature-extracting algorithms to detect SAFs. To address the issues, this paper presents a detection model based on regular coupling features (RCFs). After the model is only trained by the samples in single-load circuits, it can detect SAFs under unknown multi-load circuits. To extract the RCFs, asymmetric magnetic flux is coupled by passing the live line and the neutral line through the current transformer. The coupling signals are not influenced by the multi-load circuits. According to the unique signals, two time-domain features and one frequency-domain feature are extracted to represent the RCFs, including impulse - factor analysis (IFA), covariance-matrix analysis (CMA) and multiple frequency-band analysis (MFA). Then, the impulse factor and its threshold are used to preprocess the signals and decrease analysis complexity for the classifier. Finally, the experimental results show that the proposed method has significantly improved generalization ability and detection accuracy in SAF detection.

**Index Terms**—AC SAF, CMA, generalization ability, IFA, MFA, RCF

## I. INTRODUCTION

AC series arc faults (SAFs) are commonly caused by poor connection between electrical contacts, damaged wire insulation and improper operation of household appliances. When SAFs occur, they can release massive heat, resulting in extremely high temperature that could be over thousands of degrees Celsius [1]. Furthermore, circuit breakers are often difficult to be activated by SAFs because the root mean square (RMS) of the arcing current is typically lower than that of the normal current. Therefore, the failure in detection of SAFs can easily lead to fire hazards. According to the newest data collected by the U.S Fire Administration, residential fire accidents account for 76.17% in all the fires and are the leading type for fire deaths (72.2%), fire injuries (76.4%) and economic loss (46.4%) [2]. Among the residential fire accidents, the fires resulting from electrical system relating causes occupy a major proportion. The same data also suggest that, from 2009 to the present, the electrical fire trend remains nearly unchanged, and there is no sign of significant decline in such incidents. Therefore, some effective measures should be taken to prevent fire hazards from SAFs. To detect SAFs, it has been specified in the standard IEC62606 that the arc fault detection device

(AFDD) should correctly identify SAFs under some required types of loads, e.g. resistive loads, dimmer loads, etc. Furthermore, AFDD is also required to work in some specific combination of load types, where four configurations named *A*, *B*, *C* and *D* are defined in [3]. However, arcing current features could be significantly different in different types of circuits and loads. In residential buildings, there are not only the aforementioned four configurations as defined in [3], but also multi-branch circuits and various different fault types, which will make SAF detection extremely difficult. In addition to these issues, the detection will be more challenging when some non-linear loads and resistive loads are connected to the circuit. For instance, the non-arcing features (i.e. normal behavior) of the non-linear loads are very similar to the arcing features, and the arcing features in the resistive loads are not obvious.

In recent years, more and more researchers have paid attention to AC SAF detection and proposed many algorithms to extract effective arcing features by trunk-line current [4-6]. They can be divided into two main categories: traditional algorithms and artificial intelligence (AI) algorithms.

In the former methods, discrete Fourier transformation (DFT) and discrete wavelet transformation (DWT) are often used to obtain distinctive indicators in a certain frequency band, where there is an obvious difference between arcing and non-arcing conditions [7-10]. The associated thresholds can then be determined to detect SAFs. Nevertheless, these algorithms may fail to work in some types of loads, e.g. cleaners, dimmers, etc., because their non-arcing signals could distribute across a wide frequency range, which can easily be confused as the arcing signals. To address this issue, reference [11] has attempted to identify SAFs through combining time-domain and frequency-domain analysis, which includes the analysis of the mean value of two subsequent current spectra, the difference between the maximum values of the spectra, the mean value of the spectrum and the current difference. Reference [12] has proposed two indicators to detect various types of high-impedance arc faults, where the first one is the global randomness index based on the unified harmonic energy, while the other is the zero-crossing period extracted by Db4-based DWT. Reference [13] has calculated the RMS value of the current signals in the time domain and average amplitude in the frequency domain respectively to identify SAFs. It can be seen from the aforementioned references that it is of critical importance to extract arcing features in both the time domain and the frequency domain because arcing current features are difficult to be detected by only a kind of indicators.

In the second category of methods based on AI algorithms,

the samples and their known results (labels) are used to obtain a desirable classification model, which will be able to perform the classification task after it learns corresponding knowledge. In the last several years, AI algorithms, e.g. support vector machine (SVM), neural network (NN), etc., have been widely investigated for fault diagnosis due to their powerful learning capacity [14-16]. Reference [17] has proposed to extract twelve kinds of current features to train SVM for distinguishing between arcing and non-arcing conditions. To simplify the structure of the input vector, principal component analysis (PCA) is applied to simplify the 12-dimensional vector down to a 3-dimensional one. Reference [18] has used fourteen features to judge the load type, based on which the SVM is trained by these features to detect whether there is an arc. During training, the best hyperparameters in the SVM are confirmed by the particle swarm optimization algorithm. Reference [19] has transformed the input current data into a series of sparse coefficients, which are fed into NN for SAF identification. It shows that the proposed sparse representation and fully connected neural network (SRFCNN) can correctly identify the type of load and two different conditions (i.e. arcing or not) with different types of loads. Reference [20] has analyzed wavelet energy mean, current fluctuation degree and effective value of current, and used them as the input of back propagation NN. Reference [21] has mapped the time series of current to the two-dimensional gray image. It tries to extract more arcing features in order to identify arcs in various loads. Since SAFs are difficult to detect, some papers have also made attempt to obtain unique arcing features other than electrical quantities, e.g. light and heat. However, they are limited to the location where SAFs occur [22-24]. Therefore, the existing works still suggest that the SAF current detection is a more promising approach.

In the latest techniques, there is manual feature extraction and deep learning-based feature extraction. The former category includes time-domain analysis and frequency-domain analysis. Then the extracted features are classified by the self-defined thresholds or the classifier. The latter one refers to the end-to-end frameworks, e.g. convolutional NN and recurrent NN, without manual feature extraction [16]. However, there are still many challenging issues in AC series arc fault detection. The arcing current features are always influenced by circuit types, load types and fault inception points. Furthermore, the normal current signals also have fault-like features, e.g. zero crossing, high rates of rise after zero crossing, etc., in many load. In the latest works, the current signals in the known circuits are analyzed. Then the corresponding features are extracted to distinguish between arcing current and normal current [4]. It is widely considered that these methods could be in high risk of failure in fault detection when a new load or a new multi-load circuit is present. Even if the algorithms are improved by adjusting the thresholds or the algorithm structure in order to solve misjudgment in some new circuits, the revised algorithms could fail again in other new conditions because there are countless types of current signals in AC series arc fault detection.

Different from the recent works, this paper proposes a SAF detection strategy based on regular coupling features (RCFs). The contributions are listed as follows:

1) To address the issue that the changing current features influence the generalization performance of the recent works

[4], this paper further shows the signals of single-load circuits are quite similar to those of multi-load circuits by a coupling method. The special phenomena make it possible to detect SAFs under unknown multi-load circuits. Few references discuss how to detect SAFs under unknown circuits.

2) However, there is a vital limitation in the coupling method. The normal coupling signals of the dimmer loads are confused as the arcing ones. Therefore, three RCFs are used to further enhance the generalization performance of the coupling method. The proposed detection strategy is based on the RCFs and only required to be trained by the samples in single-load circuits. The strategy can detect SAFs under unknown multi-load circuits. Furthermore, it can also guarantee high detection accuracy when new loads are present in the circuit.

3) Different from the recent SAF detection methods based on AI algorithms, the proposed method does not require high-dimensional features and load classification, and it achieves 99.4% detection accuracy among 18000 samples from unknown load combinations and various kinds of faults.

The main idea in this paper can be summarized as follows. A coupling method is used to acquire signals by passing the live line and the neutral line through the current transformer. Three representative features are extracted, including two time-domain features and one frequency-domain one. One time-domain feature is extracted by impulse factor analysis (IFA), and the other is extracted by covariance matrix analysis (CMA). The frequency-domain feature is extracted by multiple frequency-band analysis (MFA). To decrease the input-vector dimensions and analysis complexity, IFA can be used to firstly judge whether the samples are non-arcing. Then, the classifier is trained by the normalized vector, which is composed of CMA and MFA. Therefore, the brief detection strategy is as follows. Firstly, the sample is processed by IFA and its threshold. If its IFA value is smaller than the threshold, it must be normal. Otherwise, the sample with suspected SAFs needs to be further judged by the trained SVM for a final decision.

The rest of the paper is structured as follows. In section II, the principle of the coupling method is introduced, and the coupling method is compared with the traditional method to demonstrate it has stronger capability in extracting weak arcing signals. In section III, the coupling method shows the signal relationship under arbitrary circuits, and the advantages of the selected models are clarified theoretically when the models are used to extract the RCFs. In section IV, the classifier is trained by the samples in single-load circuits. Then, the trained model is verified by off-line analysis and on-line detection, respectively. It is found that the proposed model can work not only in single-load circuits, but also in unknown multi-load circuits. Finally, it is compared with other methods to show its better generalization performance. In section V, conclusions of this work on SAF detection are present.

## II. PRINCIPLE OF THE COUPLING METHOD

In Fig. 1, this paper has applied a coupling method to detect SAFs instead of the traditional current detection method. The coupling method is that the neutral line and the live line are passed through the current transformer to obtain the coupling signals. Different from the leakage current detection, the proposed method couples the high-frequency asymmetric

magnetic flux instead of the current amplitude difference [25].

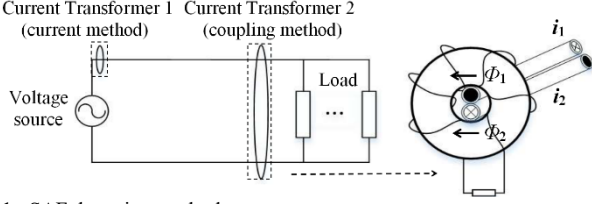


Fig. 1. SAF detection method.

Firstly, the current function can be expanded as follows according to Fourier series:

$$i_1(t) = -i_2(t) = \frac{a_0}{2} + \sum_{n=1}^{\infty} [a_n \cos(n\omega t) + b_n \sin(n\omega t)] \quad (1)$$

$$a_n = \frac{2}{T} \int_{t_0 - \frac{T}{2}}^{t_0 + \frac{T}{2}} i_1(t) \cos(n\omega t) dt, \quad b_n = \frac{2}{T} \int_{t_0 - \frac{T}{2}}^{t_0 + \frac{T}{2}} i_1(t) \sin(n\omega t) dt \quad (2)$$

where  $\omega$  is the angular frequency, and  $T$  is the signal period. The formulas of trigonometric functions are used to simplify the above equation:

$$i_1 = -i_2 = \sum_{n=0}^{\infty} A_n \sin(n\omega t + \varphi_n) \quad (3)$$

$$A_0 \sin \varphi_0 = \frac{a_0}{2} \quad (4)$$

$$A_n = \sqrt{a_n^2 + b_n^2}, \quad \varphi_n = \arctan \frac{a_n}{b_n}, \quad n = 1, \dots, \infty \quad (5)$$

When the live line and the neutral line are passed through the current transformer whose aperture only accommodates two cables, the relationship between the current and its corresponding magnetic flux can be expressed as follows:

$$\phi_1 = \sum_{n=0}^{\infty} l_n^+ A_n \sin(n\omega t + \varphi_n) \quad (6)$$

$$\phi_2 = \sum_{n=0}^{\infty} l_n^- A_n \sin(n\omega t + \varphi_n) \quad (7)$$

where  $l_n^+$  and  $l_n^-$  are the linear factors. Since the positions of the two cables are not symmetric,  $l_n^+$  is not absolutely equal to  $l_n^-$ . Therefore, the output of the transformer can be expressed as:

$$u = N \frac{d(\phi_1 - \phi_2)}{dt} = N \frac{d(\sum_{n=0}^{\infty} \chi_n A_n \sin(n\omega t + \varphi_n))}{dt} \quad (8)$$

where  $N$  is the coil turns, and  $\chi_n$  is equal to  $l_n^+ - l_n^-$ . Then,  $\chi_n$  is replaced with a small-value constant  $\chi$  because the range of  $\chi_n$  is small. The equation (8) can be approximately written as follows:

$$u \approx N\chi \frac{d(\sum_{n=0}^{\infty} A_n \sin(n\omega t + \varphi_n))}{dt} = N\chi \frac{di}{dt} = \gamma \frac{di}{dt} \quad (9)$$

When there is no SAF in the circuit, there will be very small high-frequency components in the line current for most loads, which will make  $\gamma$ , a very small value, predominate in  $u$ . Therefore, the variation of the normal coupling signals will be approximately 0. On the contrary, there are abundant high-frequency pulses in the line current when SAFs occur, and the arcing pulses will weaken the influence from  $\gamma$  to a large extent by the derivative operation in the equation (9). Therefore, the

arcing coupling signals can clearly show the impulsive feature, and they will fluctuate significantly.

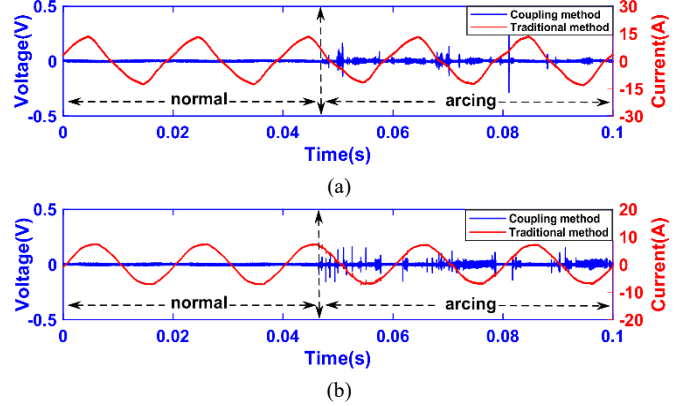


Fig. 2. Waveform before and after arcs acquired by the traditional current method and the coupling method. (a) The circuit with an air compressor and a 5A resistance. (b) The circuit with a desktop and a 5A resistance.

To compare the coupling method with the traditional method, Fig. 2 shows the signal-acquisition results before and after arcs. In the traditional current detection method, there is almost no difference between arcing currents and normal ones. However, with the coupling method, even weak arcing features can be extracted from heavy current. Meanwhile, the method can still also achieve classification between arcs and no arcs under arbitrary circuits. In the time domain, the arcing coupling signals show abundant pulses, whereas the normal coupling signals show few pulses. This effectively addresses the issue that arcing features often change or vanish in the traditional current detection method.

In Table I, a quantitative parameter is used instead of Fig. 2 to better evaluate the ability of the proposed coupling method and the traditional method in distinguishing arcing and non-arcing conditions. The parameter is defined as follows:

$$\delta_E = \frac{E_{arc} - E_{nor}}{E_{arc}} \times 100\%, \quad E = \sum_{i=1}^n data_i^2 \quad (10)$$

where  $E$  is the signal energy.  $E_{arc}$  represents the arcing signal energy, and  $E_{nor}$  represents the normal signal energy.  $data_i$  is the value of the  $i^{th}$  sample. When there is a distinct difference between arcing signals and normal ones under a certain method, the difference value between arcing energy ( $E_{arc}$ ) and normal energy ( $E_{nor}$ ) is expected to be large, which also makes  $\delta_E$  large. Therefore, a larger absolute value of  $\delta_E$  means a better identification performance. In the table,  $|\delta_E|$  of the coupling method (78.91%) is almost ten times as big as that of the traditional method (7.88%), which indicates the coupling method has significantly improved identification performance in SAF detection.

TABLE I  
A PARAMETER TO EVALUATE THE PERFORMANCE BETWEEN DIFFERENT METHODS

Signal-acquisition method	$ \delta_E $	Identification performance
Coupling method	78.91%	Excellent
Traditional current method	7.88%	Bad

### III. REGULAR COUPLING FEATURES AND SAF DETECTION ALGORITHMS

In Fig. 3 and Fig. 4, the coupling signals before and after arcs are shown under the resistive load (5A resistance), the inductive

load (air compressor) and the non-linear loads (dimmer and fluorescent lamp), respectively. Under the non-dimmer circuits, the arcing signals show abundant pulses, and the non-arcing ones are stable without pulses. Unlike the non-dimmer loads, when the dimmer load is connected to the circuit, there are also high-frequency pulses in the coupling signals during normal operation as shown in Fig 3 (d) and Fig 4 (d).

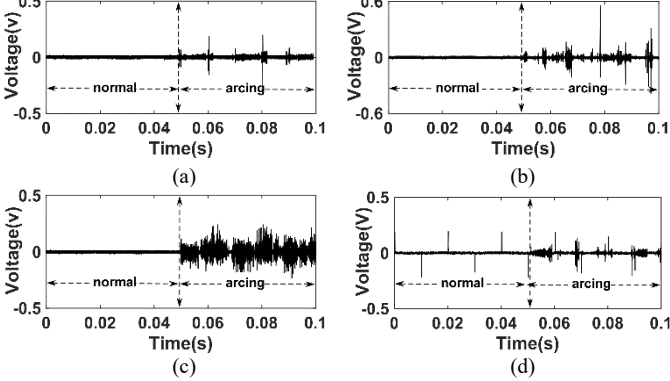


Fig. 3. Regular coupling features in time domain. (a) 5A resistance. (b) Air compressor. (c) Fluorescent lamp. (d) Dimmer load.

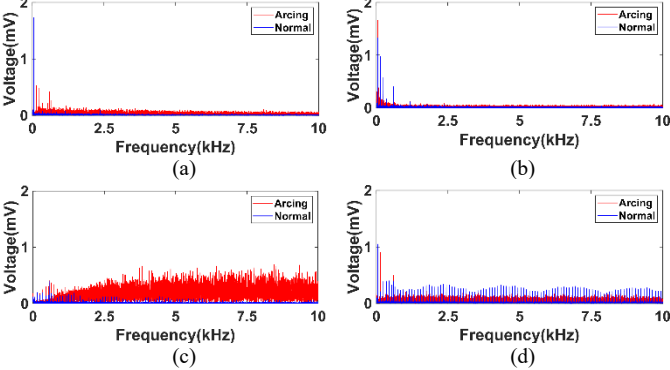


Fig. 4. Frequency-domain signals of Fig. 3 (a) 5A resistance. (b) Air compressor. (c) Fluorescent lamp. (d) Dimmer load.

Therefore, the normal output under arbitrary circuits without the non-dimmer load is:

$$u_{nor}^{(1)} = \gamma \frac{d[\sum_{k=1}^h i_k(t)]}{dt} \approx \gamma h \frac{di_e}{dt} \approx 0 \quad (11)$$

$$\gamma \frac{di_e}{dt} = \gamma \sum_{n=0}^{m_1} n \omega A_n \cos(n\omega t + \varphi_n) \approx 0 \quad s.t. \quad \gamma \omega A_n \approx 0, \text{ for } \forall n=1, \dots, m_1 \quad (12)$$

where  $i_e$  represents the normal current of the non-dimmer load, and there are  $h$  branches.  $m_1$  represents the largest harmonic number of the non-dimmer current. The normal output under arbitrary circuits with the dimmer load is:

$$u_{nor}^{(2)} = \gamma \frac{d[\sum_{k=1}^h i_k(t)]}{dt} = \gamma(h-1) \frac{di_e}{dt} + \gamma \frac{di_d}{dt} \approx \gamma \frac{di_d}{dt} \neq 0 \quad (13)$$

$$\begin{aligned} \gamma \frac{di_d}{dt} &= \gamma \sum_{n=0}^{m_1} n \omega A_n \cos(n\omega t + \varphi_n) + \gamma \sum_{n=m_1+1}^{m_2} n \omega A_n \cos(n\omega t + \varphi_n) \\ &\approx \gamma \sum_{n=m_1+1}^{m_2} n \omega A_n \cos(n\omega t + \varphi_n) \neq 0 \end{aligned} \quad (14)$$

where  $i_d$  represents the normal current of the dimmer.  $m_2$  ( $> m_1$ ) represents the largest harmonic number of the dimmer

current. On the contrary, the line current contains a large number of high-frequency components when SAFs occur. The arcing output under arbitrary circuits is:

$$u_{arc} \neq 0 \quad (15)$$

All the equations above show the coupling signals of multi-load circuits share the similar features with those of single-load circuits. Therefore, it is not necessary to analyze the signals in complex multi-load circuits. The RCFs make it possible to detect SAFs under unknown load combinations by only analyzing the signals of single-load circuits. The RCFs can be divided into two categories. The first category is the signals without pulses. When there are no arcs in the non-dimmer circuits, the coupling signals belong to the category. The other category is the signals with pulses, including the normal signals of the dimmer circuits and the arcing ones of all the circuits. The idea of the signal analysis based on the RCFs is shown in Fig. 5. According to the RCFs, three representative algorithms are used to discriminate between the arcing signals and the non-arcing ones, including impulse-factor analysis (IFA), covariance-matrix analysis (CMA) and multiple frequency-band analysis (MFA). IFA can be firstly used to separate the non-pulse signals (①) from the pulse signals (② and ③). Then, CMA and MFA can be used to distinguish between ② and ③. The preprocessing method based on IFA can decrease analysis complexity for the SAF detection because the remaining task is only to analyze the pulse signals regardless of the non-arcing signals of the non-dimmer loads.

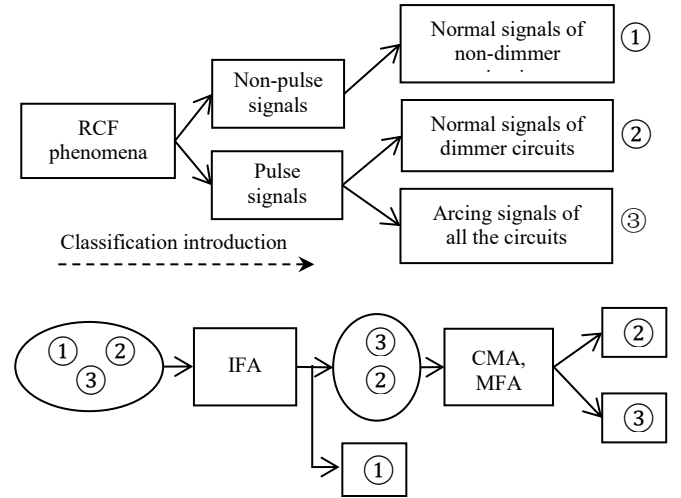


Fig. 5. RCF phenomena and corresponding classification process.

### A. Impulse Factor Analysis

IFA is considered to be an effective method to distinguish between the non-pulse signals and the pulse ones because the ratio of the maximum value to the mean value is sensitive to the pulse signals. The calculation for the algorithm can be described as follows:

$$IFA = \frac{\max(|u_1|, \dots, |u_N|)}{\frac{1}{N} \sum_{i=1}^N |u_i|} \quad (16)$$

where  $N$  is the number of samples, and  $u_1, \dots, u_N$  are the samples. Assuming the  $N$  samples include  $n_1$  stable samples and  $n_2$  pulse samples. When there are no pulses in the coupling signals, all

the absolute values are very small and defined as  $A$ . When there are pulses, some values are much bigger than  $A$  and defined as  $B$ . The mean values of the non-pulse signals ( $MV_1$ ) and the pulse signals ( $MV_2$ ) are expressed as follows:

$$MV_1 = \frac{n_1 \cdot A + n_2 \cdot B}{(n_1 + n_2)} = A, n_1 = N \text{ and } n_2 = 0 \quad (17)$$

$$MV_2 = \frac{n_1 \cdot A + n_2 \cdot B}{(n_1 + n_2)} = \frac{n_1}{(n_1 + n_2)} A + \frac{n_2}{(n_1 + n_2)} B \approx A, n_1 \gg n_2 \quad (18)$$

According to the above-mentioned equations, the IFA value of the pulse signals is much bigger than that of the stable signals:

$$\frac{\max_1}{MV_1} < \frac{\max_2}{MV_2} \quad (19)$$

where  $\max_1$  and  $\max_2$  are the maximum absolute values of the stable coupling signals and the impulsive coupling signals, respectively. Meanwhile, compared with the maximum-value indicator, IFA is less vulnerable to the influence of the unit. For example, when the coupling signals are magnified  $k$  times, the IFA value of the impulsive coupling signals is still bigger than that of the stable coupling signals. However, the maximum-value indicator fails to follow the rule:

$$\frac{\max_1}{MV_1} = \frac{k \cdot \max_1}{k \cdot MV_1} < \frac{\max_2}{MV_2} = \frac{k \cdot \max_2}{k \cdot MV_2} \quad (20)$$

$$\max_1 < \max_2 < k \cdot \max_1 < k \cdot \max_2 \quad (21)$$

### B. Multiple Frequency-band Analysis

The non-arcing pulses in the dimmer loads have the periodic characteristic and appear approximately every 10 ms. They are often confused as the arcing ones in the time domain. To address the issue, the difference between the non-arcing pulses and the arcing ones is analyzed by the frequency-domain transformation algorithm. The function of the non-arcing pulses is defined as  $f(t)$  and expressed as follows by the trigonometric functions and the Euler's formula:

$$\begin{aligned} f(t) &= \frac{a_0}{2} + \sum_{n=1}^{\infty} [a_n \cos(\omega_n t) + b_n \sin(\omega_n t)] \\ &= \frac{a_0}{2} + \sum_{n=1}^{\infty} \left[ \frac{a_n - ib_n}{2} e^{i\omega_n t} + \frac{a_n + ib_n}{2} e^{-i\omega_n t} \right] \\ &= \frac{1}{T} \sum_{n=-\infty}^{+\infty} \left[ \int_{t_0 - \frac{T}{2}}^{t_0 + \frac{T}{2}} f(t) e^{-i\omega_n t} dt \right] e^{i\omega_n t} \end{aligned} \quad (22)$$

Then, the periodic function can be expressed as the following form by the frequency-domain transformation algorithm:

$$\begin{aligned} F(\omega) &= \frac{1}{T} \sum_{n=-\infty}^{+\infty} \left[ \int_{t_0 - \frac{T}{2}}^{t_0 + \frac{T}{2}} f(t) e^{-i\omega_n t} dt \right] e^{i\omega_n t} \cdot e^{-i\omega t} dt \\ &= \frac{1}{T} \sum_{n=-\infty}^{+\infty} \left[ \int_{t_0 - \frac{T}{2}}^{t_0 + \frac{T}{2}} f(t) e^{-i\omega_n t} dt \right] \cdot \int_{-\infty}^{+\infty} e^{i\omega_n t} \cdot e^{-i\omega t} dt \end{aligned} \quad (23)$$

According to the inverse transformation algorithm, the frequency-domain form of  $e^{i\omega_n t}$  can be written as:

$$\begin{aligned} e^{i\omega_n t} &= \frac{1}{2\pi} \int_{-\infty}^{+\infty} F_1(\omega) \cdot e^{i\omega t} d\omega \\ &= \frac{1}{2\pi} \int_{-\infty}^{+\infty} 2\pi \delta(\omega - \omega_n) \cdot e^{i\omega t} d\omega \end{aligned} \quad (24)$$

$$\int_{-\infty}^{+\infty} e^{i\omega_n t} \cdot e^{-i\omega t} dt = F_1(\omega) = 2\pi \delta(\omega - \omega_n) \quad (25)$$

where  $\delta()$  is the Dirac delta function. Therefore, the final

expression of  $f(t)$  in the frequency domain can be obtained by combining all the equations above:

$$F(\omega) = \frac{1}{T} \sum_{n=-\infty}^{+\infty} \left[ \int_{t_0 - \frac{T}{2}}^{t_0 + \frac{T}{2}} f(t) e^{-i\omega_n t} dt \right] \cdot 2\pi \delta(\omega - \omega_n) \quad (26)$$

The non-arcing pulses tend to show the same phenomenon in the frequency spectrum, where there is a pulse in each frequency band. On the contrary, there are no pulse features in the frequency domain of most fault signals. The function of the fault signals is defined as  $g(t)$ , and the corresponding transformation can be obtained as follows:

$$F(\omega) = \lim_{T \rightarrow \infty} \int_{t_0 - \frac{T}{2}}^{t_0 + \frac{T}{2}} g(t) e^{-i\omega t} dt \quad (27)$$

$$= \int_{-\infty}^{+\infty} g(t) e^{-i\omega t} dt, \lim_{T \rightarrow \infty} \bar{g}(t) = g(t) \text{ and } \lim_{T \rightarrow \infty} n\omega = \omega$$

To extract the feature, the spectrum is obtained as follows:

$$A(\omega) e^{i\phi(\omega)} = \int_{-\infty}^{+\infty} \sum_{n=0}^{N-1} u(t) \delta(t - nT_s) e^{-\frac{2\pi}{NT_s} t} dt = \sum_{n=0}^{N-1} u(nT_s) e^{-\frac{2\pi}{N} n} \quad (28)$$

$$A(k\omega) e^{i\phi(k\omega)} = \sum_{n=0}^{N-1} u(nT_s) e^{-\frac{2\pi}{N} nk}, k \in [0, N-1] \quad (29)$$

where  $N$  is the number of samples,  $k$  is the harmonic order,  $i$  is the imaginary number, and  $T_s$  is the sampling period.  $A(\omega)$  is the signal amplitude, and  $e^{i\phi(\omega)}$  is the signal phase.  $u(t)$  is the coupling signals. Assuming the normal pulses distribute in a frequency band ( $A_{a+1}, A_{a+2}, \dots, A_{a+b}$ ), which is divided into  $c$  bands with equal width (there are  $w$  points in each band). Since there is a pulse in each band, an algorithm is used here to extract the spectral pulse. For example, the algorithm in the first band ( $A_{a+1}, \dots, A_{a+w}$ ) is expressed as follows:

$$Z_1 = \frac{\max([A_{a+1}, \dots, A_{a+w}])}{\frac{1}{w} \sum_{i=1}^w A_{a+i}} \quad (30)$$

Then, all the elements in the sequence  $[Z_1, \dots, Z_c]$  are added up to represent the degree of fluctuation in the whole band (from  $A_{a+1}$  to  $A_{a+b}$ ). Therefore, MFA can be written as follows:

$$MFA = \sum_{j=0}^{c-1} \left( \frac{\max([A_{a+1+jw}, \dots, A_{a+w+jw}])}{\frac{1}{w} \sum_{i=1}^w A_{a+i+jw}} \right) \quad (31)$$

### C. Covariance-matrix Analysis of Time Series

The number of arcing pulses in some non-linear loads and inductive loads is more than the number of non-arcing pulses in the dimmer loads, which indicates that the former features are more abundant. To reasonably extract these arcing pulses, covariance-matrix analysis of the time-series matrix is adopted in this work. One of the covariance-matrix functions is that its eigenvectors can transfer the corresponding time-domain signals into many regions, and each region represents one feature. The time series is reconstructed by the eigenvectors whose eigenvalues are put in a descending order.

Assuming the time series is composed of  $N$  samples:  $u_1, u_2, \dots, u_N$ . The time-series matrix  $T_{L \times M}$  ( $N=L \times M$ ) is written as:

$$[u_1, u_2, \dots, u_{N-1}, u_N] \rightarrow T_{L \times M} = \begin{bmatrix} u_1 & \cdots & u_{L(M-1)+1} \\ \vdots & \ddots & \vdots \\ u_L & \cdots & u_N \end{bmatrix} \quad (32)$$

Then, the mean-subtraction operation should be performed in

each column of  $T$ :

$$\hat{T} = \begin{bmatrix} u_1 - \frac{1}{L} \sum_{i=1}^L u_i & \cdots & u_{L(M-1)+1} - \frac{1}{L} \sum_{i=1}^L u_{L(M-1)+i} \\ \vdots & \ddots & \vdots \\ u_L - \frac{1}{L} \sum_{i=1}^L u_i & \cdots & u_N - \frac{1}{L} \sum_{i=1}^L u_{L(M-1)+i} \end{bmatrix} = \begin{bmatrix} \hat{u}_1 & \cdots & \hat{u}_{L(M-1)+1} \\ \vdots & \ddots & \vdots \\ \hat{u}_L & \cdots & \hat{u}_N \end{bmatrix} \\ = [\vec{t}_1, \cdots, \vec{t}_L]' \quad (33)$$

where  $[\ ]'$  is the transposed matrix of  $[\ ]$ . Assuming that  $\vec{V}$  ( $=[v_1, \dots, v_M]$ ) is a unit vector. When the time-series matrix is projected onto  $\vec{V}$ ,  $S$  is defined as the total distances from the projected points to the origin. The partial time series with the most obvious feature can be obtained by maximizing  $S$ :

$$S = \frac{1}{L-1} \sum_{j=1}^L \sum_{i=1}^M (\hat{u}_{L(i-1)+j} v_i)^2 = \frac{1}{L-1} \sum_{j=1}^L (\vec{V} \vec{t}_j) (\vec{V} \vec{t}_j)' \\ = \frac{1}{L-1} (\vec{V} \hat{T}' \hat{T} \vec{V}') = \vec{V} C \vec{V}' \quad (34)$$

where  $C$  is the covariance matrix. Then, the maximum  $S$  can be calculated by the Lagrange multiplier method:

$$S = \vec{V} C \vec{V}' \quad s.t. \vec{V} \vec{V}' = 1 \quad (35)$$

$$h(\lambda, \vec{V}) = \vec{V} C \vec{V}' + \lambda(1 - \vec{V} \vec{V}') \quad (36)$$

$$\frac{\partial h}{\partial \lambda} \equiv 0, \quad \frac{\partial h}{\partial \vec{V}} = 2C \vec{V}' - 2\lambda \vec{V}' = 0 \quad (37)$$

$$S = \vec{V} \lambda \vec{V}' = \lambda \quad (38)$$

The equation above indicates the larger  $\lambda$  is, the more greatly the projected points fluctuate. When the time-series matrix is reconstructed according to the eigenvectors whose eigenvalues are putting in the descending order, the dispersion degree in the reconstructed signals decreases in turn from the first reconstructed subgroup to the last one:

$$C V_i' = \lambda_i V_i', \quad i \in [1, M] \quad (39)$$

$$P_i = \hat{T} V_i', \quad i \in [1, M] \quad (40)$$

$$T_{rec} = [P_1, \dots, P_M], \quad \lambda_1 \geq \dots \geq \lambda_M \quad (41)$$

where  $P_i$  is the reconstructed subgroup.  $T_{rec}$  is the reconstructed matrix.  $V_i$  and  $\lambda_i$  are the eigenvector and the eigenvalue, respectively.  $V_i$  is obtained by the corresponding  $\lambda_i$ . Since there are a few pulses in the normal coupling signals, the pulses only distribute in the first  $N_1$  subgroups of the reconstructed signals:

$$\lambda_1 + \dots + \lambda_{N_1} \approx \lambda_1 + \dots + \lambda_{N_1} + \dots + \lambda_{N_2}, \quad N_1 < N_2 < M \quad (42)$$

There are abundant pulses in the arcing coupling signals of some loads. Therefore, the pulses distribute in more subgroups ( $N_2$  subgroups):

$$\lambda_1 + \dots + \lambda_{N_1} < \lambda_1 + \dots + \lambda_{N_1} + \dots + \lambda_{N_2}, \quad N_1 < N_2 < M \quad (43)$$

Then, CMA can be obtained by analyzing the central moment of the non-overlapping subgroups:

$$T_{rec} \xrightarrow{\text{flatten}} [u_1^r, \dots, u_N^r] \quad (44)$$

$$CMA = \frac{1}{L(N_2 - N_1)} \sum_{i=1}^{L(N_2 - N_1)} \frac{[u_{LN_1+i}^r - E([u_{LN_1+1}^r, \dots, u_{LN_2}^r])]^4}{[D([u_{LN_1+1}^r, \dots, u_{LN_2}^r])]^2} \quad (45)$$

where  $D$  is the variance operation, and  $E$  is the mean operation.

## D. Proposed Models in Detail

### (1) MFA

According to the spectral analysis of the arcing signals (an example is present in Fig. 6), it shows that the arcing information mainly distributes below 400 kHz. Therefore, the sampling rate ( $SR$ ) is selected as 1 MHz. For the observation window ( $OW$ ), it should be as short as possible because a large  $OW$  could increase computational complexity. However, the selected  $OW$  should also be long enough in order to avoid the spectrum leakage and failure in extracting the non-arcing features.

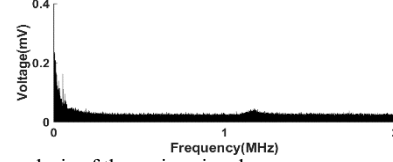


Fig. 6. Spectral analysis of the arcing signals.

In Fig. 7, different  $OW$ s (0.2 s, 0.1 s, 0.05 s) are compared, and it shows that the spectrum leakage is so serious that the spectral features almost disappear under the shortest  $OW$  (0.05 s). Finally, the  $OW$  is selected as 0.1 s (frequency resolution=10 Hz), which ensures that MFA can correctly recognize the normal pulses under the premise of the lowest computational complexity. Then, it can be seen from Fig. 7 that the spectral features appear at 100 Hz intervals. Meanwhile, they mainly distribute from 0.1 kHz to 20 kHz. According to this phenomenon, the frequency band is selected from 0.1 kHz to 20.09 kHz to better calculate the parameters. Therefore,  $a$ ,  $c$  and  $w$  in the equation (31) are 10, 200 and 10, respectively.

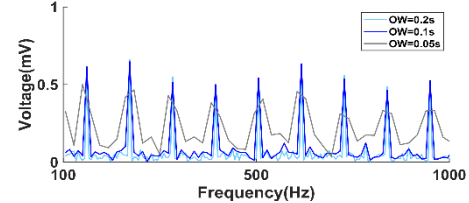


Fig. 7. Influence on the spectral analysis of the non-arcing pulses under different  $OW$ s.

### (2) CMA

According to the confirmed  $OW$  and  $SR$ , there are 100000 points in each  $OW$ , and these points make up the time-series matrix. The number of columns ( $M$ ) should be sufficiently large because it influences the ability of extracting the features. Therefore,  $N$ ,  $M$  and  $L$  are 100000, 200 and 500, respectively, in the equation (32). In Fig. 8, the time series is reconstructed by the eigenvectors of its covariance matrix, and the eigenvalues are put in a descending order. The normal pulses distribute in the first 6000 points (from  $P_1$  to  $P_{12}$ ), and the arcing pulses distribute in the first 15000 points (from  $P_1$  to  $P_{30}$ ). According to Fig. 8 (a) and (b), it is appropriate to distinguish between arcs and no arcs from the 6001<sup>th</sup> point to the 15000<sup>th</sup> point (from  $P_{13}$  to  $P_{30}$ ). Therefore,  $N_2$  and  $N_1$  are 30 and 12, respectively, in the equation (45).

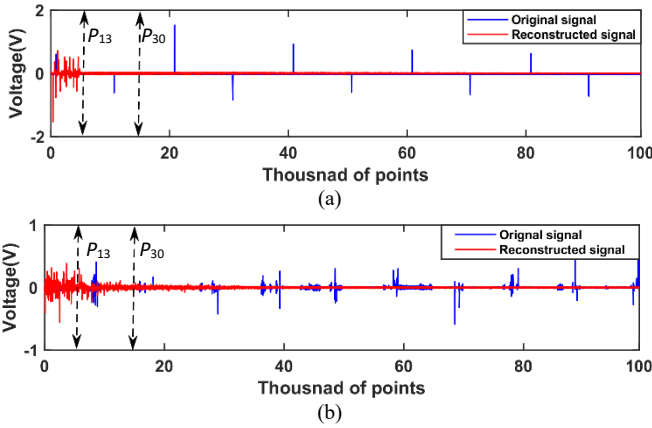


Fig. 8. Reconstructed time series by the covariance matrix. (a) Normal pulses of the dimmer loads. (b) Arcing pulses.

Fig. 9 shows the brief feature distribution diagram of the non-arcing pulses and the arcing ones. To find out the appropriate margin for CMA and MFA, the classifier is selected as SVM, and its input vector is composed of the two-dimensional vector (CMA and MFA). Its hyperplane can be used for classification and expressed as:  $\omega^T x + b = 0$ , where  $\omega$  and  $b$  are the weight and bias, respectively, and  $x$  is the input data. Finally, the brief flowchart of the detection strategy in this paper is shown in Fig. 10.

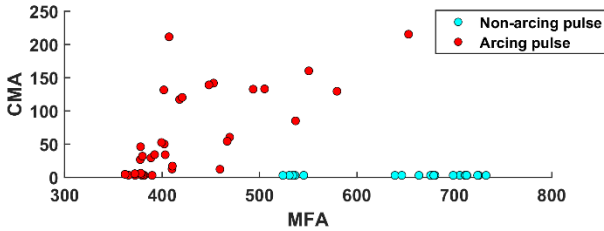


Fig. 9. Brief distribution diagram between non-arcing pulses and arcing ones.

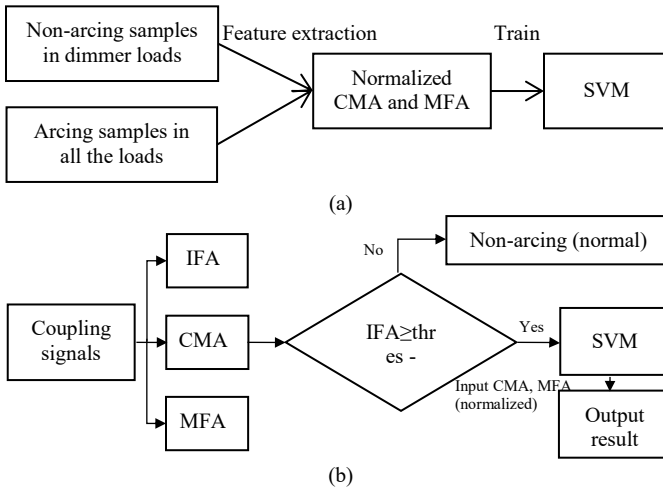


Fig. 10. SAF detection introduction. (a) Training process. (b) Detection process.

Among the three indicators, which are extracted from the coupling signals, IFA is firstly used to judge whether there is an arc. If its value is smaller than the set threshold, the detection strategy outputs the normal result. Otherwise, the further decision should be made by inputting CMA and MFA into the classifier for a final classification result. The input vector is preprocessed by the z-score normalization before being input to

the classifier to improve the convergence speed and the detection accuracy.

#### IV. EXPERIMENTAL VERIFICATION

The experimental platform is illustrated in Fig. 11 (a), where the experimental loads include the 5A resistance, the electric hand drill (240 W), the vacuum cleaner (1200 W), the air compressor (950 W), the desktop, the fluorescent lamps (80 W) and the dimmer lamps (600 W) with the  $30^\circ_{\min}$ ,  $60^\circ$ ,  $90^\circ$ , and  $120^\circ_{\max}$  firing angles, respectively. The coupling signals are acquired by the current transformer whose frequency response can reach 10 MHz. Its output is connected with a low-pass filter whose cut-off frequency is the half of the  $SR$  to suppress high-frequency noise. The proposed strategy is tested under the off-line experiment and the on-line one, respectively, to evaluate its performance. The experimental process is shown in Fig. 11 (b).

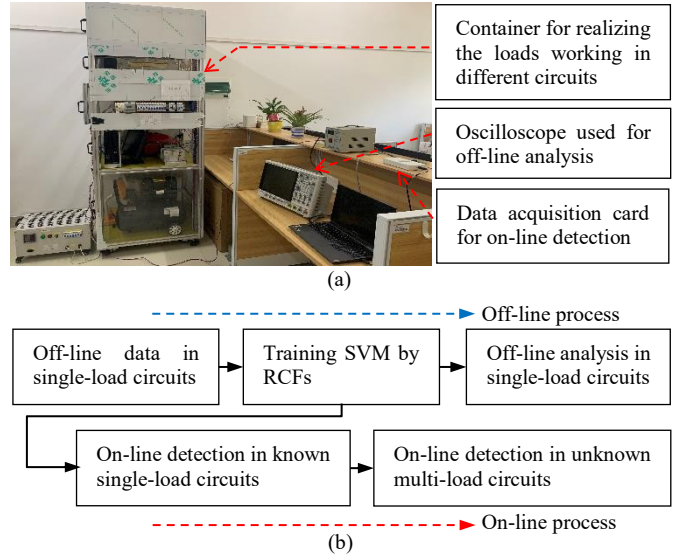


Fig. 11. Off/on-line experiment. (a) Experimental platform. (b) Experimental process.

TABLE II  
IFA VALUES UNDER DIFFERENT LOADS

Single-load circuit	Status	IFA	Threshold
Non-dimmer loads	Non-arcing ①	$3 < \text{value} < 8$	16
	Arcing ③	$\text{value} > 20$	
Dimmer loads	Non-arcing ②	$\text{value} > 20$	
	Arcing ③	$\text{value} > 20$	

Off-line analysis: the data are exported from the oscilloscope and analyzed in the computer. According to Section III, the  $OW$  and the  $SR$  are set as 0.1 s and 1 MHz, respectively. Then, the IFA results are recorded in Table II. The non-arcing values are smaller than 8 under the non-dimmer loads (5A resistance, fluorescent lamp, vacuum cleaner, drill, desktop, air compressor), and most of the arcing ones are larger than 20 under all the loads. However, the non-arcing values are also bigger than 20 under the dimmer loads. Therefore, its threshold is set as 16 to firstly separate ① from ② and ③ (①, ② and ③ in Table II are the same as ①, ② and ③ in Fig. 5, respectively).

The data set used to train SVM includes the normal samples of the dimmer loads (4 kinds: the dimmers with the  $30^\circ_{\min}$ ,  $60^\circ$ ,  $90^\circ$ , and  $120^\circ_{\max}$  firing angles, respectively) and the arcing ones of all the loads (10 kinds: the 5A resistance, the electric hand

drill, the vacuum cleaner, the air compressor, the desktop, the fluorescent lamps and the dimmer lamps with the  $30^\circ_{\min}$ ,  $60^\circ$ ,  $90^\circ$ , and  $120^\circ_{\max}$  firing angles, respectively). The normal samples of the non-dimmer loads are not added to the training set because their IFA values are smaller than the set threshold ( $=16$ ) and the detection strategy would directly output ‘normal’ instead of inputting them into the classifier. The data set is divided into two parts: the training set and the test set. The former one takes up 80% in all the samples, and the latter one takes up 20%. In the training set, the 5-fold cross validation is used to estimate the generalization ability of SVM, and the detection accuracy of the trained classifier is obtained by detecting the samples in the test set. The kernel function and its corresponding hyperparameters are temporarily fixed to observe the influence of the training-sample number on the detection accuracy. When the number of training samples is selected as 80 ( $10_{\text{kind}}*4+4_{\text{kind}}*10$ ), 160 ( $10_{\text{kind}}*8+4_{\text{kind}}*20$ ), 320 ( $10_{\text{kind}}*16+4_{\text{kind}}*40$ ), respectively, the detection accuracy is about 93.8%, 96.9% and 100%, respectively. If the number of training samples continues to increase, the hyperplane expression will remain nearly unchanged. Therefore, the number of training samples is 320 in this paper.

During the training process, the SVM structure is constantly adjusted to find out the best detection accuracy, including the kernel function and the corresponding hyperparameters. In the kernel functions, some popular kernel functions are tested, including the linear function, the Gaussian Radial Basis function and the sigmoid function. The detection accuracy can achieve 100% under the arbitrary kernel function. However, the final selection is the linear function because it is much simpler than any other functions in computation complexity. The corresponding hyperparameter ‘ $C$ ’ can be obtained by the optimization algorithm after the kernel function is determined. In the optimization algorithms, the particle swarm optimization (PSO), the genetic algorithm (GA) and the grid search (GS) are selected, respectively, to find out the desirable hyperparameter. The range of  $C$  is from 0.1 to 100. Then, in the process of optimization, no matter GS, GA or PSO can achieve the maximum detection accuracy, but  $C$  selected by GA or PSO is random for there are many solutions. In practice,  $C$  should be selected as a small value to avoid overfitting. Therefore, GS is adopted to find out the minimum  $C$  and keep the maximum detection accuracy. Finally,  $C$  is selected as 0.5. In the hyperplane expression,  $\omega$  and  $b$  are  $[-2.072852, 1.951638]$ , and 0.113886, respectively, after training.

On-line detection: the classifier is trained by the RCFs in the off-line analysis. Then it is adopted to detect the real-time data. The data are acquired by the acquisition card to achieve the on-line detection for SAFs. The detection steps follow Fig. 10 (b). In the online detection, the number of arcing test samples is 500 under each load, and the number of normal test samples is also 500 under each load. There are 10 kinds of loads in total. The on-line detection results are shown in Table III, where the proposed detection strategy is tested by different  $SR$ s, including 1 MHz, 250 kHz and 100 kHz. Finally, the results show that the minimum  $SR$ , by which the proposed strategy can work, is 250 kHz. Therefore, the  $SR$  is 250 kHz in this paper. When the  $SR$  is 100 kHz, MFA cannot separate the non-arcing pulses from the arcing ones, which results in unwanted trips in the dimmer circuits. It should be noted that the parameters in the time-series

matrix are changed when the  $SR$  is changed. For example, when the  $SR$  is 250 kHz,  $M$  and  $L$  are 50 and 500, respectively.

TABLE III  
ON-LINE DETECTION ACCURACY IN SINGLE-LOAD CIRCUITS BY DIFFERENT  $SR$ s

$SR$	Test samples	Detection accuracy
1 MHz	$10000=500*(10_{\text{normal kind}}+10_{\text{arcing kind}})$	99.7%
<b>250 kHz</b>	$10000=500*(10_{\text{normal kind}}+10_{\text{arcing kind}})$	99.6%
100 kHz	$10000=500*(10_{\text{normal kind}}+10_{\text{arcing kind}})$	59.9%

TABLE IV  
ON-LINE DETECTION ACCURACY UNDER UNKNOWN MULTI-LOAD CIRCUITS

Multi-load circuit	Class	Test samples	Detection accuracy
Dim.30°+Res.5A	Normal (1 kind)	1500 ( $1_{\text{kind}}*1500$ )	100%
	Arcing (3 kinds)	1500 ( $3_{\text{kind}}*500$ )	97%
Vac.cleaner+Res.5A	Normal (1 kind)	1500 ( $1_{\text{kind}}*1500$ )	100%
	Arcing (3 kinds)	1500 ( $3_{\text{kind}}*500$ )	99.9%
Fluo.lamp+Res.5A	Normal (1 kind)	1500 ( $1_{\text{kind}}*1500$ )	100%
	Arcing (3 kinds)	1500 ( $3_{\text{kind}}*500$ )	98.7%
Drill+Res.5A	Normal (1 kind)	1500 ( $1_{\text{kind}}*1500$ )	100%
	Arcing (3 kinds)	1500 ( $3_{\text{kind}}*500$ )	100%
Desktop+Res.5A	Normal (1 kind)	1500 ( $1_{\text{kind}}*1500$ )	100%
	Arcing (3 kinds)	1500 ( $3_{\text{kind}}*500$ )	99.7%
Air.compress+Res.5A	Normal (1 kind)	1500 ( $1_{\text{kind}}*1500$ )	100%
	Arcing (3 kinds)	1500 ( $3_{\text{kind}}*500$ )	97.1%
<b>Overall detection accuracy under unknown multi-load circuit:</b>			<b>99.4%</b>

TABLE V  
PRECISION, RECALL AND F1-SCORE UNDER UNKNOWN MULTI-LOAD CIRCUITS

	Arcing	Normal	Total
Arcing	8886	114	9000
Normal	0	9000	9000
Total	8886	9114	18000
Precision=100%		Recall= 98.7%	F1-score=99.3%

The appropriate extraction of arcing features is a vital issue because arcing features in the traditional current detection method change with different circuits and fault inception points. As discussed previously in Section III, the coupling signals show that they would not be influenced by multi-load circuits, and there are the RCFs between single-load circuits and multi-load ones. The on-line detection accuracy under unknown load combinations is shown in Table IV, which proves the feasibility of the proposed method. In each circuit, the arcing kinds include the branch faults (2 kinds) and the trunk fault (1 kind). The overall detection accuracy can reach about 99.4% (18000 samples). Among the 0.6% failure-to-trip samples, they are almost similar to the non-arcing samples, which is shown in Fig. 12, and their IFA values distribute from 3 to 8. Therefore, they are classified into the non-arcing samples. To further evaluate the performance of the proposed method, a confusion matrix is produced and shown in Table V. The precision, recall and F1-score are 100%, 98.7% and 99.3%, respectively. In practice, it is unbearable that the normal samples are classified into the arcing ones because a large false positive rate would make the circuit breakers trip incorrectly. Therefore, the F0.5-score is

TABLE VI  
COMPARISON WITH RECENTLY PUBLISHED ALGORITHMS

SAF detection method	Proposed method	Reference [4]	Reference [8]	Reference [17]	Reference [18]	Reference [26]
Main part of detection algorithm	Extracting regular coupling features	CNN based on raw current signals	Singular value decomposition	NN-based load classification and SVM-based SAF detection		Fourth order cumulant
Feature size	3	5000	1	12	14	1
Number of load type	10	3 (used as an example)	8	5		10
Detection accuracy (single-load circuits)	99.6%	99.8%	93.8%	99.3%	95.5%	90%
Detection accuracy (unknown multi-load circuits)	99.4%	71.6%	66.7%	The reference states its SAF detection method based on load classification cannot work in multi-load circuits.		83.3%

also calculated. Its value is 99.7% and indicates that the proposed method can avoid unwanted trips very well.

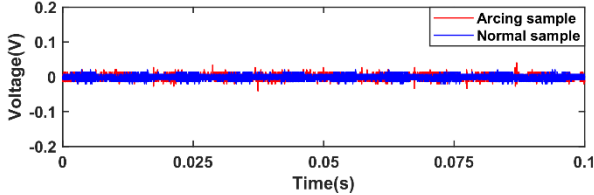


Fig. 12. The reason of failure to trip in Table IV.

In Table VI, the proposed method is compared with recently published algorithms. Recently, CNN has achieved excellent detection accuracy in fault diagnosis, however, a supersize training set is required when CNN is applied in complex circuits. Since the acquired features are different under different fault inception points and load combinations, there are various kinds of waveforms. Under this circumstance, the training set may need to be composed of over billions of points, not to mention the usage of data augmentation. To avoid this issue, the authors tried to train CNN with the samples in single-load circuits, and used the trained CNN to detect SAFs under unknown load combinations. To simplify the comparison, the samples in three kinds of loads are used to train CNN. According to reference [4], the input vector of CNN is the raw current signals. The selected structure contains 6 convolutional layers (activation function: ReLU, filters (kernel size): 64 (3), 32 (3), 16 (3), 8 (3), 4 (3) and 2 (3), respectively), 6 maxpooling layers (pool size (stride): 2 (2), 3 (2), 2 (2), 3 (2), 2 (2) and 3 (2), respectively.) and 5 full connected layers (final-layer activation function: Softmax, neurons: 512, 256, 256, 128 and 2, respectively). However, the detection results are not satisfactory in the multi-load circuits (800 samples). Reference [8] has used short-observation-window singular value decomposition and reconstruction to filter out the interference pulses. Then, variance energy is calculated based on the reconstructed signals. The detection strategy cannot work in the halogen lamps because the normal energy of the halogen lamps is confused as the arcing energy of other loads.

Reference [26] has adopted the fourth-order cumulant algorithm to detect arcing pulses by the sampling rate of 10 MHz. However, the normal pulses would result in unwanted trips under the dimmer loads because the method cannot discriminate between normal pulses and arcing ones. Reference [17] and [18] have used PCA-SVM and PSO-SVM, respectively, to detect SAFs. To improve the detection accuracy, they have to complex the dimensions of the input vector and recognize the load types before detecting because the arcing and

normal current features are quite different among different loads, and a low-dimensional feature vector is not sufficient to detect SAFs. In addition to complicated calculation, these kinds of methods based on SVM cannot be used in multi-load circuits because they require load classification. Therefore, the proposed method based on the RCFs has not only better detection accuracy in single-load circuits, but generalization ability in unknown multi-load circuits. Although the proposed method requires more calculation time than the simple time-domain method of reference [26] because of the eigenproblem and frequency-domain analysis, the detection accuracy of the proposed method is much better than that of reference [26]. Table VI shows three features are extracted by the proposed method to detect SAFs, including IFA, CMA and MFA. IFA and its corresponding threshold are firstly used to separate the non-pulse signals from the pulse signals because the non-pulse signals are normal. Therefore, SVM is only trained by a two-dimensional vector (CMA and MFA) instead of a high-dimensional one to decrease analysis complexity.

In this paper, a simple test is also made to further evaluate the generalization ability of the proposed method. A random one of the 10 arcing loads is removed from the training set but still kept in the test set. The changed model can still guarantee the same detection accuracy as the original one. Furthermore, the proposed method can also work very well in unknown single-load circuits, including the halogen lamps, the microwave oven, the energy-saving lamps, the hair dryer, the kettle and the refrigerator.

## V. CONCLUSION

To address the issue that arcing current features change or vanish under different load-combination modes and fault inception points, this paper proposes a RCF-based detection model. The model is only trained by the samples in single-load circuits and can detect SAFs under unknown multi-load circuits. The coupling signals adopted by the proposed method are largely unaffected by multi-load circuits, and there are RCFs between single-load circuits and multi-load circuits. Furthermore, the time-domain and frequency-domain analysis, CMA, IFA and MFA, can extract the RCFs correctly. When the  $SR$  is selected as 250kHz, its overall detection accuracy is 99.4% (18000 samples) under unknown load combinations. Compared with other existing detection methods, the proposed method can not only detect SAFs under more kinds of loads with higher detection accuracy, but also shows significantly stronger generalization performance in detecting SAFs under unknown multi-load circuits.

## REFERENCES

- [1] M. Ahmadi, H. Samet and T. Ghanbari, "Series Arc Fault Detection in Photovoltaic Systems Based on Signal-to-Noise Ratio Characteristics Using Cross-Correlation Function," *IEEE Transactions on Industrial Informatics*, vol. 16, no. 5, pp. 3198-3209, May 2020.
- [2] U.S. Fire Administration. Residential and nonresidential building fire and fire loss estimates by property use and cause (2003-2019).
- [3] "General requirements for arc fault detection devices," *IEC62606*, Apr. 2014.
- [4] Y. Wang, L. Hou, K. C. Paul, Y. Ban, C. Chen and T. Zhao, "ArcNet: Series AC Arc Fault Detection Based on Raw Current and Convolutional Neural Network," *IEEE Transactions on Industrial Informatics*, vol. 18, no. 1, pp. 77-86, Jan. 2022.
- [5] Y. Wang, F. Zhang, X. Zhang and S. Zhang, "Series AC Arc Fault Detection Method Based on Hybrid Time and Frequency Analysis and Fully Connected Neural Network," *IEEE Transactions on Industrial Informatics*, vol. 15, no. 12, pp. 6210-6219, Dec. 2019.
- [6] M. K. Khafidli, E. Prasetyono, D. O. Anggriawan, A. Tjahjono and M. H. Riza Alvi Syafii, "Implementation AC Series Arc Fault Recognition using Mikrokontroler Based on Fast Fourier Transform," 2018 International Electronics Symposium on Engineering Technology and Applications (IES-ETA), Bali, 2018, pp. 31-36.
- [7] N. Qu, J. Wang and J. Liu, "An Arc Fault Detection Method Based on Current Amplitude Spectrum and Sparse Representation," *IEEE Transactions on Instrumentation and Measurement*, vol. 68, no. 10, pp. 3785-3792, Oct. 2019.
- [8] R. Jiang, G. Bao, Q. Hong and C. D. Booth, "A Coupling Method for Identifying Arc Faults Based on Short-Observation-Window SVDR," *IEEE Transactions on Instrumentation and Measurement*, vol. 70, pp. 1-10, 2021.
- [9] X. Qin, P. Wang, Y. Liu, L. Guo, G. Sheng, and X. Jiang, "Research on distribution network fault recognition method based on time-frequency characteristics of fault waveforms," *IEEE Access*, vol. 6, pp. 7291-7300, 2018.
- [10] H. Ji, G. Wang, W. Kim, G. Kil, "Optimal Design of A Band Pass Filter and an Algorithm for Series Arc Fault Detection," *Energies*, vol. 11, no. 4, Apr. 2018.
- [11] G. Artale, A. Cataliotti, V. Cosentino, D. Di Cara, S. Nuccio and G. Tinè, "Arc Fault Detection Method Based on CZT Low-Frequency Harmonic Current Analysis," *IEEE Transactions on Instrumentation and Measurement*, vol. 66, no. 5, pp. 888-896, May 2017.
- [12] M. Wei et al., "High Impedance Arc Fault Detection Based on the Harmonic Randomness and Waveform Distortion in the Distribution System," *IEEE Transactions on Power Delivery*, vol. 35, no. 2, pp. 837-850, April 2020.
- [13] K. Zeng, L. Xing, Y. Zhang and L. Wang, "Characteristics analysis of AC arc fault in time and frequency domain," 2017 Prognostics and System Health Management Conference (PHM-Harbin), Harbin, 2017, pp. 1-5.
- [14] M. El Koujok, A. Ragab, H. Ghezzaz and M. Amazouz, "A Multiagent-Based Methodology for Known and Novel Faults Diagnosis in Industrial Processes," *IEEE Transactions on Industrial Informatics*, vol. 17, no. 5, pp. 3358-3366, May 2021.
- [15] Q. Guo, Y. Li, Y. Song, D. Wang and W. Chen, "Intelligent Fault Diagnosis Method Based on Full 1-D Convolutional Generative Adversarial Network," *IEEE Transactions on Industrial Informatics*, vol. 16, no. 3, pp. 2044-2053, March 2020.
- [16] W. Li, Y. Liu, Y. Li and F. Guo, "Series Arc Fault Diagnosis and Line Selection Method Based on Recurrent Neural Network," *IEEE Access*, vol. 8, pp. 177815-177822, 2020.
- [17] J. Jiang et al., "Series Arc Detection and Complex Load Recognition Based on Principal Component Analysis and Support Vector Machine," *IEEE Access*, vol. 7, pp. 47221-47229, 2019.
- [18] N. Qu, J. Zuo, J. Chen and Z. Li, "Series Arc Fault Detection of Indoor Power Distribution System Based on LVQ-NN and PSO-SVM," *IEEE Access*, vol. 7, pp. 184020-184028, 2019.
- [19] Y. Wang, F. Zhang and S. Zhang, "A New Methodology for Identifying Arc Fault by Sparse Representation and Neural Network," *IEEE Transactions on Instrumentation and Measurement*, vol. 67, no. 11, pp. 2526-2537, Nov. 2018.
- [20] X. Han, D. Li, L. Huang, H. Huang, J. Yang, Y. Zhang, X. Wu, and Q. Lu, "Series Arc Fault Detection Method Based on Category Recognition and Artificial Neural Network," *Electronics*, vol. 9, no. 9, pp. 1367, Aug. 2020.
- [21] R. Chu, P. Schweitzer, R. Zhang, "Series AC Arc Fault Detection Method Based on High-Frequency Coupling Sensor and Convolution Neural Network," *Sensors*, vol. 20, no. 17, pp. 4910, Aug. 2020.
- [22] G. Wang, W. Kim, H. Ji, G. Kil, "Detection and Analysis of series arc using non-conventional methods in low-voltage switchboards," *Journal of electrical engineering-elektrotechnicky casopis*, vol. 69, no. 4, pp. 317-322, Aug. 2018.
- [23] L. Zhao, Y. Zhou, K. Chen, S. Rau and W. Lee, "High-Speed Arcing Fault Detection: Using the Light Spectrum," *IEEE Industry Applications Magazine*, vol. 26, no. 3, pp. 29-36, May-June 2020.
- [24] P. Parikh, D. Allcock, R. Luna and J. Vico, "A Novel Approach for Arc-Flash Detection and Mitigation: At the Speed of Light and Sound," *IEEE Transactions on Industry Applications*, vol. 50, no. 2, pp. 1496-1502, March-April 2014.
- [25] G. Bao, R. Jiang and X. Gao, "Novel Series Arc Fault Detector Using High-Frequency Coupling Analysis and Multi-Indicator Algorithm," *IEEE Access*, vol. 7, pp. 92161-92170, 2019.
- [26] G. Bao, R. Jiang and D. Liu, "Research on Series Arc Fault Detection Based on Higher-Order Cumulants," *IEEE Access*, vol. 7, pp. 4586-4597, 2019.



**Run Jiang** received the B.S. and M.S. degrees from Fuzhou University, Fujian, China, in 2016 and 2020, respectively, where he is currently pursuing the Ph. D. degree. His main research interest is the detection of arc faults and partial discharge.



**Guanghai Bao** (corresponding author) received the B.S. and Ph.D. degrees in electrical engineering from Fuzhou University, Fujian, China, in 2000 and 2011, respectively. He was a post-doctorate at Changshu switching Manufacturing Co.,Ltd. He is currently an associate professor in the College of Electrical Engineering, Fuzhou University, Fujian, China. His research interests mainly include electrical appliances and fault diagnosis.



**Qiteng Hong** (S'11-M'15-SM'22) is currently a Senior Lecturer (Associate Professor) at the University of Strathclyde, Glasgow, U.K. His main research interest is on power system protection and control in future networks with high penetration of renewables. He received his B.Eng. (Hons) and Ph.D. degree in Electronic and Electrical Engineering in 2011 and 2015 respectively, both from the University of Strathclyde. Dr Hong is a member of IEEE Working Group P2004 and IEEE Task force on Cloud-Based Control and Co-Simulation of Multi-Party Resources in Energy Internet, and he also was a Regular Member of the completed CIGRE WG B5.50.



**Campbell D. Booth** received the B.Eng. and Ph.D. degrees in electrical and electronic engineering from the University of Strathclyde, Glasgow, U.K., in 1991 and 1996, respectively. He is currently a Professor and the Head of the Department for Electronic and Electrical Engineering, University of Strathclyde. His research interests include power system protection; plant condition monitoring and intelligent asset management; applications of intelligent system techniques to power system monitoring, protection, and control; knowledge management; and decision support systems.